Pergamon

Int. J. Heat Mass Transfer. Vol. 41, No. 14, pp. 2183–2195, 1998

Printed in Great Britain
0017–9310/98 $19.00+0.00

PII: S0017–9310(97)00302–5

A nucleate boiling model for structured enhanced surfaces

LIANG-HAN CHIEN and RALPH L. WEBB†
Department of Mechanical Engineering, The Pennsylvania State University, University Park, PA 16802, U.S.A.

(*Received* 23 *April* 1997 *and in final form* 26 *September* 1997)

Abstract—Flow visualization experiments were used to establish the mechanism of boiling on enhanced surfaces having sub-surface tunnels with surface pores. Based on this mechanism, a semi-analytical model for nucleate boiling is proposed. The model is validated for data covering a range of tunnel and pore dimensions and supporting bubble dynamics data. The model assumes the tunnel is vapor filled, except liquid menisci in the corners. By analyzing meniscus thickness, bubble departure diameter, and bubble growth, this dynamic model accounts for the temporal evaporation rate variation inside tunnels, and the dynamic nature of convection heat transfer outside the tunnels. The model uses two empirical constants. It predicts the heat transfer coefficient for the R-11, R-123, R-134a and R-22 pool boiling data with MSD = 20%. It also predicts bubble departure diameter and bubble frequency with MSD = 7 and 15%, respectively. © 1998 Elsevier Science Ltd. All rights reserved.

INTRODUCTION

Nucleate boiling is an important mode of heat transfer. Although commercially made enhanced boiling surfaces are used in the refrigeration and process industries, there is considerable lack of understanding of the boiling mechanism, and of knowledge to predict the effect of the geometric parameters and fluid properties on performance. The present work is part of a major study directed at providing the missing information. Chien and Webb [1, 2] and Chien [3] have performed series of tests to determine the effects of geometric parameters for the boiling performance of a 'structured' enhanced surface. This geometry consists of a finned tube whose fins are covered by a foil having small pores that allow liquid inlet and vapor release. The liquid–vapor conditions in the tunnel, and bubble growth above the surface pore were established by bubble dynamic experiments (Chien and Webb [4]) and visualization experiments (Chien and Webb [5]) using a high speed photographic system. Based on the data and observations from these experiments, the authors propose a semi-analytical model for boiling on structured surfaces.

Prior to the present work, Nakayama *et al.* [6] and Haider [7] also proposed mechanistically based analytical models to predict boiling performance of structured enhanced surfaces. Nakayama *et al.* [6] proposed that three possible boiling mechanisms may exist. These are the 'flooded mode', the 'suction–evaporation mode', and the 'dried-up mode'. The Nakayama *et al.* [6] model assumed evaporation on menisci in the corners of the tunnel (suction–evaporation mode). The Haider [7] model is based on the 'flooded mode,' which assumes alternate zones of liquid slugs and vapor plugs in the sub-surface tunnels. Observations by Nakayama *et al.* [8], Arshad and Thome [9], Chien and Webb [5] confirm the Nakayama *et al.* [6] model is correct for saturated boiling.

Nakayama *et al.* [6] assumed that the total heat flux from structured surfaces is the sum of the following two parts.

(1) Tunnel heat flux (q''_{tun}) due to to the thin-film evaporation inside the tunnels of the enhanced surface.
(2) Sensible heat flux (q''_{ex}) due to the external convection induced by bubble agitation.

Both fluxes are based on the projected surface area. This is expressed by the following equation.

$$q'' = q''_{\mathrm{tun}} + q''_{\mathrm{ex}}. \tag{1}$$

Their dynamic model is based on the sequence of events during one complete cycle of bubble growth and departure. According to the tunnel pressure and bubble growth conditions, they divided one bubble cycle into three phases: 1. pressure build-up phase, 2. pressure reduction phase, 3. liquid-intake phase. The temporal variation of the liquid meniscus thickness during a bubble cycle was ignored in their model.

In the Nakayama *et al.* [6] model, the external convection heat flux does not include the bubble frequency and bubble departure diameter. Ayub and Bergles [10] used the empirical Nakayama *et al.* [6] external heat flux model, which requires a correlation of the nucleation site density, and assumed the tunnel

---

† Author to whom correspondence should be addressed.

NOMENCLATURE

A	surface area [m^2]
A_{tun}	total surface area inside tunnels
A_{m}	meniscus surface area [m^2]
b	constant used in equation (23)
Bo	bond number, $Bo = [d_p^2(\rho_l - \rho_v)g]/\sigma$
c	empirical constant in the external heat flux, dimensionless
c_{p}	heat capacity [J (g-K)$^{-1}$]
C_{b}	empirical constant of the bubble departure diameter, dimensionless
C_{H}	Hamaker constant [J]
C_{Rm}	empirical constant in the $R_{\mathrm{m,i}}$ correlation $(\mathrm{kg\ s^{-1}})^{1.771}/(\mathrm{N}^{0.512}\ \mathrm{m}^{1.358}\ \mathrm{K}^{1.882})$
C_{tl}	empirical constant for the tunnel heat transfer rate in waiting period [cm]
C_{tg}	empirical constant used for the model of bubble growth period, dimensionless
d_{b}	bubble departure diameter [m]
$d_{\mathrm{b,exp}}$	bubble departure diameter from the experimental data [m]
$d_{\mathrm{b,pred}}$	bubble departure diameter predicted by the present model [equation (19)] [m]
d_{p}	pore diameter [m]
$\mathrm{d}Q_{\mathrm{m}}/\mathrm{d}t$	heat transfer rate to a meniscus [J s^{-1}]
f	bubble frequency [s^{-1}]
f_{exp}	bubble frequency from the experimental data [s^{-1}]
fins m	fins per meter
f_{pred}	bubble frequency predicted by the present model [s^{-1}]
F_{B}	buoyancy force [N]
F_{s}	surface tension force [N]
g	acceleration due to gravity [m s^{-2}]
h	heat transfer coefficient [W (m^2-K)$^{-1}$]
H_{t}	tunnel height [m]
i_{fg}	latent heat [J kg^{-1}]
k	thermal conductivity [W (m-K)$^{-1}$]
k_{l}	thermal conductivity of liquid [W (m-K)$^{-1}$]
L	tunnel length [m]
m	slope of P_{s} vs. T_{s} ($m = \mathrm{d}P/\mathrm{d}T$)
m_{v}	vapor mass [kg]
MSD	mean square deviation
n	exponents
$n1$–$n5$	exponents used in the $\Delta A_{\mathrm{l,cyc}}$ correlation, dimensionless
n_{s}	nucleation site density [l m^{-2}]
N_{m}	number of menisci exist in each tunnel
P	pressure [Pa]
P_{f}	fin pitch [m]
P_{l}	liquid pressure [Pa]
P_{p}	pore pitch [m]
Pr	Prandtl number, dimensionless
P_{s}	pressure of the saturated pool liquid [Pa]
P_{t}	tunnel pitch [m]
P_{v}	vapor pressure [Pa]
q''	heat flux [W m^{-2}]
q''_{DHF}	dry-out heat flux [W m^{-2}]
$q''_{\mathrm{ex,MR}}$	external heat flux defined by equation (29) [W m^{-2}]
q''_{ex}	external heat flux [W m^{-2}]
q''_{exp}	total heat flux from the experimental data [W m^{-2}]
q''_{pred}	total heat flux predicted by the present model [W m^{-2}]
q''_{tun}	tunnel heat flux [W m^{-2}]
Q_{bub}	latent heat for a departing bubble [J]
Q_{m}	heat evaporated from liquid menisci [J]
Q''_{m}	heat evaporated from liquid menisci in a bubble cycle [J]

Q_{tun}	total latent heat evaporated in the tunnel during a bubble cycle, equation (10) [J]
r	radius of meniscus interface curvature [m]
R	radius [m]
R_{b}	tunnel base radius [m]
R_{g}	gas constant [J (g-K)$^{-1}$]
R_{m}	meniscus radius [m]
$R_{\mathrm{m,A}}$	meniscus radius at Section A–A (Fig. 5) [m]
$R_{\mathrm{m,B}}$	meniscus radius at Section B–B (Fig. 5) [m]
$R_{\mathrm{m,i}}$	meniscus radius at the beginning of a bubble cycle (Fig. 1) [m]
$R_{\mathrm{m,g}}$	meniscus radius at the beginning of the growth period (Fig. 1) [m]
$R_{\mathrm{m,e}}$	minimum meniscus radius at the end of a bubble cycle (Fig. 1) [m]
R_{ne}	non-evaporation meniscus radius, defined by equation (2) [m]
R_{p}	pore radius [m]
s	coordinate along the liquid–vapor interface
s_{g}	surface gap width [m]
t	time [s]
t_{a}, t_{b}, t_{c}, t_{d}	periods during bubble growth shown in Fig. 1
T	temperature [K]
T_{l}	liquid temperature [K]
T_{s}	saturation temperature [K]
T_{v}	vapor temperature [K]
T_{vl}	vapor temperature at the end of waiting period [K]
T_{vo}	vapor temperature in the tunnel at the beginning of the waiting period [K]
T_{w}	wall temperature [K]
T_{w}^{*}	reference wall temperature, shown in equations (25)
u	velocity of the liquid in the tunnel [m s^{-1}]
$u_{s,\mathrm{ave}}$	average liquid velocity in the s direction [m s^{-1}]
$u_{x,\mathrm{ave}}$	average liquid velocity in the x direction [m s^{-1}]
V_{b}	bubble volume [m^3]
V_{t}	tunnel volume ($V_{\mathrm{t}} = L \cdot W_{\mathrm{t}} \cdot H_{\mathrm{t}}$) [m^3]
V_{v}	vapor volume [m^3]
V_{vl}	volume of the vapor at the end of the waiting period [m^3]
V_{vm}	average volume of the vapor during the waiting period [m^3]
W_{t}	tunnel width [m]
x	coordinate along the tunnel length
y	coordinate normal to the liquid–vapor interface.

Greek symbols

α	half angle of the bubble center to pore as defined in Fig. 3, degree
δ	liquid film thickness [m]
δ_{m}	meniscus thickness [m]
δ_{ne}	non-evaporation liquid film thickness [m]
$\Delta A_{\mathrm{l,cyc}}$	change of liquid cross-section area during a bubble cycle [equation (31)] [m^3]
ΔP_{br}	break through pressure ($\Delta P_{\mathrm{br}} = 4\sigma/d_{\mathrm{p}}$) [Pa]
ΔQ_{m}	change of evaporation heat during a bubble cycle [J]
Δt	difference of time [s]
Δt_{e}	liquid intake period [s]
Δt_{g}	bubble growth period [s]
ΔT_{tl}	difference of the tunnel temperature during the waiting period [s]
ΔT_{vs}	difference of the saturation and the vapor temperatures ($T_{\mathrm{v}} - T_{\mathrm{s}}$) [K]

Δt_w	bubble waiting period [s]
ΔT_{ws}	difference of the saturation and the tube wall temperature [K]
$\Delta V'_{liq}$	change of liquid volume during one time step [equation (12)] [m^3]
θ	contact angle, defined in Fig. 3, degree
μ	viscosity [kg (m^2 s)$^{-1}$]
μ_l	viscosity of the liquid [kg (m^2 s)$^{-1}$]
ρ_l	liquid density [kg m^{-3}]
ρ_v	vapor density [kg m^{-3}]
ρ_{vm}	average vapor density during the waiting period [kg m^{-3}]
σ	surface tension [N m^{-1}]
ϕ	angle defined in Fig. 2
∂	partial differential.

Subscripts

b	bubble
ex	external
exp	experimental
g	growth period
l	liquid
m	meniscus
ne	non-evaporation
new	index for a new time step in equation (11)
old	index for an old time step in equation (11)
p	pore
pred	prediction
s	saturation
v	vapor
w	tube wall.

heat transfer rate is a constant. This approach does not account for the temporal variation of heat transfer in the tunnel. As discussed by Haider [7], the bubble frequency and departure diameter are important factors for external heat flux. Haider and Webb [11] have formulated an external heat flux model based on transient micro-convection, which accounts for the bubble diameter and frequency. Chien and Webb [4] show applicability of this model to the present structured surfaces.

The present dynamic model accounts for the temporal evaporation rate variation inside tunnels by analyzing meniscus thickness, bubble departure diameter, bubble growth, and the transient convection outside the tunnels.

PHYSICAL MODEL

The total heat flux can be separated into two parts, tunnel heat flux (q''_{tun}) and external heat flux (q''_{ex}) as given by equation (1). The heat transfer rate in the tunnel is governed by evaporation of liquid menisci. The external heat flux is contributed by transient conduction and convection caused by the departing bubbles.

A bubble cycle includes three periods: waiting period (Δt_w), bubble growth period (Δt_g) and liquid intake period (Δt_e).

Boiling process

Figure 1 shows the process of evaporation in the tunnel during a boiling cycle. A bubble cycle includes the following three periods:

(1) Waiting period (Δt_w): in this period, liquid is evaporated in the tunnel. However, the vapor is constrained inside the tunnel by the surface tension on the pore. Bubble embryos protrude from the pores when the vapor pressure is greater than the break through pressure of the pore ($\Delta P_{br} = 4\sigma/d_p$). Figure 1(a) and (b) show the beginning and the end of the waiting period, respectively. The liquid vapor interface is shown by the solid line. The radius of the meniscus decreases from $R_{m,i}$ at the beginning of the cycle [Fig. 1(a)] to $R_{m,g}$ at the end of this period [Fig. 1(b)]. During this period, the tunnel is filled with vapor except for the liquid menisci in the corners.

(2) Bubble growth period (Δt_g): in this period, vapor passes through surface pores and increases the bubble radius. Bubble growth is controlled by the inertia force of the liquid surrounding the bubble and the superheated vapor generated in the tunnel. The basis of this assumption is discussed in Chien and Webb [4, 5]. At the beginning of this period [Fig. 1(b)], vapor embryos having radius $R = d_p/2$, protrude from surface pores. Because the liquid in the tunnel evaporates, the radius of the meniscus changes from $R_{m,g}$ to $R_{m,e}$. Note that the effective evaporation temperature increases as the meniscus radius decreases, because the surface tension on the menisci increases the saturation pressure of the liquid menisci. No evaporation will occur on the meniscus if the elevation of saturation temperature due to capillary pressure (σ/R) of the meniscus equals the wall superheat. Therefore, the meniscus radius at the end of this period, $R_{m,e}$, should be no less than non-evaporation radius, R_{ne}, defined by

$$R_{ne} = \frac{\sigma}{\Delta T_{ws}}\left(\frac{dT}{dP}\right). \tag{2}$$

At the end of this period [Fig. 1(c)], bubbles having radius $R = d_b/2$ depart from the surface pores. The present model also assumes that the bubble shape is spherical before a bubble departs.

(3) Liquid intake period (Δt_e): after the bubble departs, liquid flows into the tunnel, and is retained in the corners. In a very short period after the bubble departs, the pressure in the tunnel is lower than that of the liquid pool. Therefore, liquid flows into the tunnel during this liquid intake period. At the end of the liquid intake period, the radius of the meniscus equals $R_{m,i}$ as shown on Fig. 1(d). The surface pore and tunnel dimensions control the amount of the liquid in the tunnel and the liquid meniscus radius. As

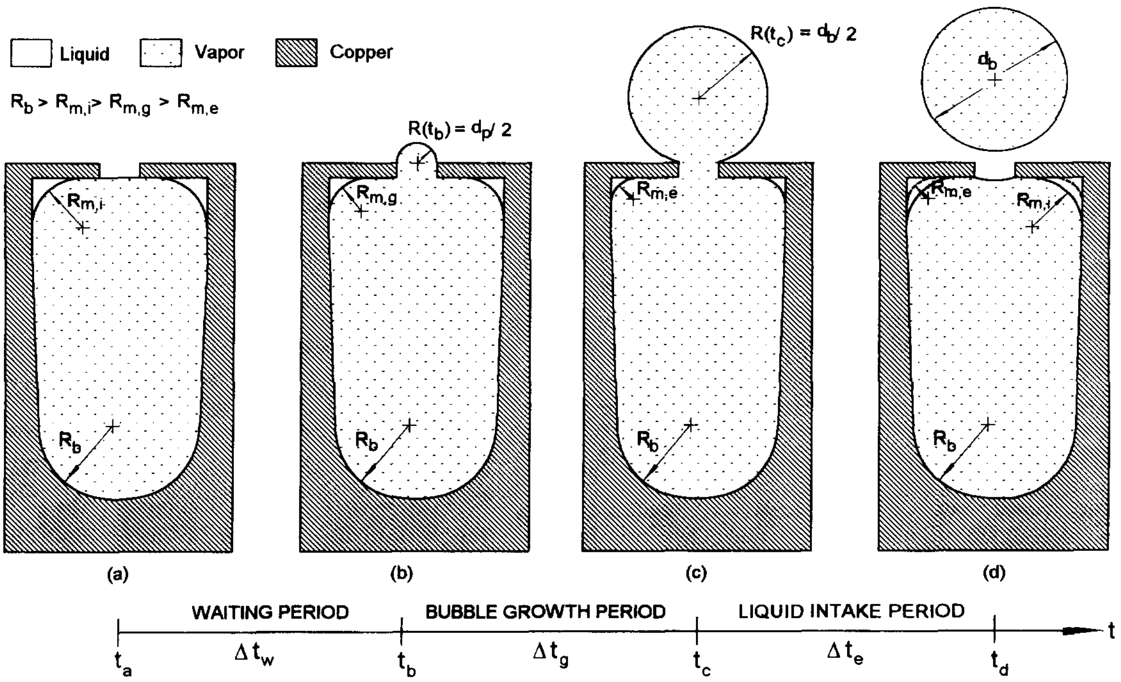

Fig. 1. Process of evaporation in the subsurface tunnel and bubble growth.

observed by Nakayama *et al.* [8], and Chien and Webb [4], this period is much shorter than the other two periods. Therefore, this period is neglected in the calculation of bubble frequency.

Assumptions for tunnel heat transfer

1. The tunnels are vapor filled, except for liquid menisci in the corners.
2. The distribution of the liquid menisci is uniform along the tunnel length.
3. The latent heat of the vapor bubbles is by evaporation inside the tunnels. Evaporation of the micro layer above the subsurface tunnel is neglected.
4. The evaporation rate is predicted by one-dimensional conduction heat transfer from the liquid meniscus region.
5. For a rectangular tunnel cross-section, liquid menisci exist in each of the four corners. For circular fin base tunnels, only two liquid menisci occur in the corners—near the fin tips.
6. For high thermal conductivity fins (e.g., copper), the wall temperature is constant over the fin height.

MATHEMATICAL MODEL

Formulation of tunnel heat flux

Based on the above physical model, the tunnel heat flux is the produce of the latent heat transferred at the menisci during a bubble cycle and the bubble frequency, as given by

$$q''_{\text{tun}}A_{\text{tun}} = (Q''_{\text{m}})f \tag{3}$$

where Q''_{m} is the latent heat from menisci in one bubble cycle. Assuming one-dimensional heat conduction in the liquid, the heat flux is given by

$$q'' = \frac{k_1}{\delta}(T_{\text{w}} - T_{\text{s}}). \tag{4}$$

In equation (4), T_{s} is the saturation temperature. When the liquid meniscus becomes very thin, the saturation temperature elevates because of the disjoining pressure and capillary pressure (σ/R). The elevation of saturation temperature due to the capillary pressure is significant when the meniscus radius (R_{m}) is very small. DasGupta *et al.* [12] assumed a power-law dependency of the disjoining pressure on δ. Experimentally, they found the disjoining pressure = (C_{H}/δ^3) for R-113, where the Hamaker constant (C_{H}) is 2.0×10^{-12} J for R-113. Accounting for the effect of capillary pressure and disjoining pressure on the liquid menisci, the equivalent saturation temperature (T_{s}), in equation (4) is given by

$$T_{\text{s}} = T_1\left(1 + \frac{\sigma/R + C_{\text{H}}/\delta^3}{i_{\text{fg}}\rho_1}\right). \tag{5}$$

The present model assumes $C_{\text{H}} = 2.0 \times 10^{-12}$ J for all the refrigerants in the present work. The authors also found that the differences of prediction on total heat transfer coefficient (h), by changing $C_{\text{H}} = 2.0 \times 10^{-11}$ to $C_{\text{H}} = 2.0 \times 10^{-13}$ J, are less than 2%.

The latent heat transfer rate at the menisci ($\text{d}Q_{\text{m}}/\text{d}t$) is given by

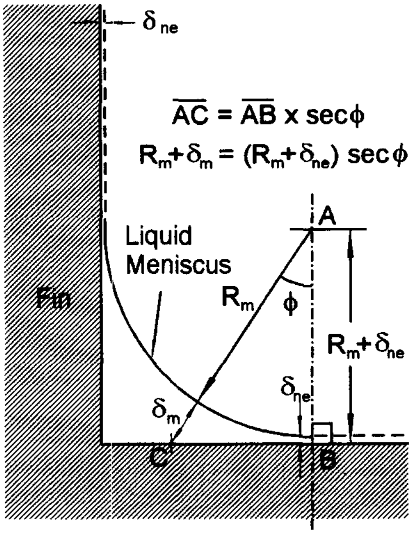

Fig. 2. Liquid meniscus thickness.

$$\frac{dQ_m}{dt} = \Delta T_{ws} \int_0^{A_m} \frac{k_l}{\delta_m(t,\phi)} dA \tag{6}$$

where $\delta_m(t,\phi)$ is the local thickness of the liquid meniscus, and A_m is the meniscus surface area measured from the interface per unit tunnel length. From the geometric analysis (Fig. 2) assuming R_m is independent on ϕ, the local liquid thickness on the menisci is given by $\delta_m(\phi) = (R_m + \delta_{ne}) \sec(\phi) - R_m$ for given radius R_m and angle ϕ. Because R_m is a function of time (t), $\delta_m = \delta_m(t,\phi)$, and is given by

$$\delta_m(t,\phi) = [R_m(t) + \delta_{ne}] \sec(\phi) - R_m(t) \tag{7}$$

where R_m is the liquid meniscus radius, and angle ϕ is defined in Fig. 2. The non-evaporation film thickness (δ_{ne}) is calculated by

$$\delta_{ne} = \left(\frac{C_H T_s}{\rho_l i_{fg}(T_w - T_s)} \right)^{1/3}. \tag{8}$$

The liquid menisci radius R_m changes during the boiling process as shown on Fig. 1. The non-evaporation film thickness δ_{ne} is much less than R_m. In equation (6), the surface area increment, $dA = L \cdot N_m \cdot R_m \cdot d\phi$, *where* $d\phi$ *is small angle increment*, N_m is number of menisci existing in each tunnel, and L is the total tunnel length. From equations (6) and (7), the total latent heat transfer rate is given by

$$\frac{dQ_m}{dt} = \Delta T_{ws} \left[2LN_m \times \int_0^{\pi/4} \frac{k_l}{[R_m(t) + \delta_{ne}(t)] s(\phi) - R_m(t)} R_m(t)\, d\phi \right]. \tag{9}$$

The total latent heat in the tunnel during one bubble cycle is given by

$$Q_{tun} = \int_0^{1/f} \frac{dQ_m}{dt} dt \tag{10}$$

where dQ_m/dt is given by equation (9). The integrations in equations (9) and (10) were numerically calculated using small increments of time (t) and angle (ϕ). The $R_m(t)$ is updated to a new value, $R_{m,new}$, for each new time step. From a geometric analysis, the $R_{m,new}$ is given by

$$R_{m,new} = \left[R_{m,old}^2 + \frac{\Delta V_{liq}}{LN_m(1 - \pi/4)} \right]^{0.5} \tag{11}$$

where ΔV_{liq} is the change of liquid volume during a time step. From mass and energy balances, one finds $\Delta V_{liq} = \Delta Q_m / (i_{fg}\rho_l)$. The $R_{m,old}$ is the meniscus radius of the previous time step. From equation (9), the volume of liquid ΔV_{liq} evaporated on the menisci during one time step (Δt) is given by

$$\Delta V_{liq} = \Delta t \frac{2LN_m \Delta T_{ws}}{i_{fg}\rho_l} \times \int_0^{\pi/4} \frac{k_l}{[R_m(t) + \delta_{ne}(t)] \sec(\phi) - R_m(t)} R_m(t)\, d\phi. \tag{12}$$

This calculation for integration of equations (9)–(12) starts from the initial meniscus radius at the beginning of the bubble cycle [$R_m = R_{m,i}$ on Fig. 1(a)] and stepwise decreases for a small time step (Δt) until $R_m = R_{m,e}$ [Fig. 1(c)].

The initial meniscus radius $(R_{m,i})$ depends on the amount of liquid that flows into the tunnel during a bubble cycle. From geometric analysis, $R_{m,i}$ is given by

$$R_{m,i} = \left[R_{m,e}^2 + \frac{\Delta A_{l,cyc}}{N_m(1 - \pi/4)} \right]^{0.5} \tag{13}$$

where $\Delta A_{l,cyc}$ is the change of the cross section area of the liquid menisci during a bubble cycle and N_m is the number of menisci per tunnel. Detailed prediction of $R_{m,i}$ or $\Delta A_{l,cyc}$ requires complex analysis involving the nucleation site density and liquid flow rate in the liquid intake period. The authors chose a simplified method, which involves correlation of $\Delta A_{l,cyc}$ based on experimental data in Chien and Webb [1–3, 13]. The development of a correlation for $\Delta A_{l,cyc}$ will be discussed later.

Modeling bubble departure diameter

From a force balance, Nakayama *et al.* [6] developed an empirical correlation, given by

$$d_b = C_b \left(\frac{2\sigma}{(\rho_l - \rho_v) g} \right)^{1/2} \tag{14}$$

to predict the bubble departure diameter on structured surfaces. Their analysis assumed that the buoyancy force equals the surface tension force in an opposite direction, and neglected the inertia force of vapor bubble. In equation (14), the empirical constant C_b was established from the Nakayama *et al.* [6] experimental data. For R-11, they chose $C_b = 0.42$, while for water $C_b = 0.22$. Their force balance analysis is supported by the analysis on plain surface by Kolev [14], who showed that only static mechanical equilibrium governs the bubble departure for plain surfaces.

Haider [7] proposed the following expression for the constant C_b in equation (14),

$$C_b = (3s_g \sin\theta)^{1/3}\left(\frac{2\sigma}{(\rho_l-\rho_v)g}\right)^{-1/6} \quad (15)$$

where θ is the contact angle. However, the contact angle θ must be established.

According to the Chien and Webb [4, 5] observations using a high speed video camera on the boiling tests of methanol, R-11 or R-123, the typical bubble shape is spherical on the structured surfaces. We assumed that the bubble shape above an active pore is spherical, and that the bubble attaches to the surface pore during the bubble growth. By a geometrical analysis, the angle α equals angle θ as shown in Fig. 3. Hence, the contact angle θ can be evaluated by

$$\theta = \sin^{-1}\left(\frac{d_p}{d_b}\right). \quad (16)$$

The buoyancy force on the bubble is given by $F_B = (\rho_l-\rho_v)gV_b$, where V_b is the volume of this bubble, given by

$$V_b = \pi\frac{d_b^3}{12}\left(1+\cos(\theta)+\frac{\cos(\theta)\sin^2(\theta)}{2}\right). \quad (17)$$

The surface tension force on the pore is given by $F_s = \sigma\pi d_p \sin(\theta)$. The balance between buoyancy and surface tension forces gives

$$\sigma d_p \sin(\theta) = (\rho_l-\rho_v)g\frac{d_b^3}{12} \times \left(1+\cos(\theta)+\frac{\cos(\theta)\sin^2(\theta)}{2}\right). \quad (18)$$

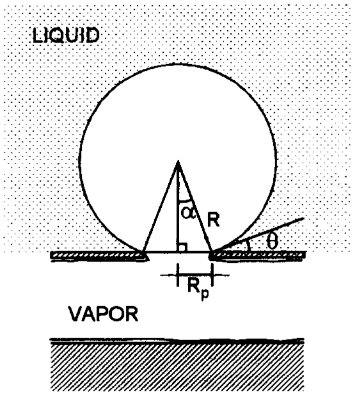

Fig. 3. Bubble growth on a surface pore.

One can rewrite equation (18) in an explicit form, given by

$$d_b = \left[\frac{Bo+\sqrt{Bo^2+2304(96/Bo-3)}}{192-6Bo}\right]^{1/2} d_p \quad (19)$$

where $Bo = [d_p^2(\rho_l-\rho_v)g]/\sigma$. Therefore, the bubble diameter d_b can be predicted by equation (19) with no empirical constant. The predictive ability of equation (19) is shown later.

Modeling bubble frequency

As described previously, a bubble cycle includes three periods. The liquid intake period is much shorter than the other two periods. Therefore, the authors assume the bubble frequency is the inverse of the summation of the waiting period (Δt_w) and the bubble growth period (Δt_g). The waiting period and the bubble growth period are modeled separately as described by the following two sections.

Waiting period. Nakayama *et al.* [6] analyzed the waiting period. From mass balance and energy balance equations, they wrote

$$\frac{1}{i_{fg}}\frac{dQ_{tun}}{dt} = \frac{dm_v}{dt} = V_v\frac{d\rho_v}{dt}+\rho_v\frac{dV_v}{dt}. \quad (20)$$

Nakayama *et al.* [6] assumed $(dQ_{tun}/dt) = C_{tl}k_l(T_w-T_v)$, where C_{tl} is a time independent empirical constant. They applied the equation of state and the Clausius–Clapeyron equation, and showed

$$\Delta t_w C_{tl} k_l = V_{vm} i_{fg}\left[\frac{\rho_v(i_{fg}-R_g T_{vo})}{R_g T_{vo}^2}\ln\left(\frac{T_w-T_{vo}}{T_w-T_{vl}}\right) + \frac{\rho_v}{\Delta T_{tl}}\ln\left(\frac{V_{vl}}{V_t}\right)\right] \quad (21)$$

where the vapor temperature (T_v), density (ρ_v) and volume (V_v) are linearized. They assume $T_{vo} = T_s$, and $V_v = V_t$ at the beginning of the waiting period. At the end of the waiting period, $T_{vl} = T_s+4\sigma/(d_p \cdot m)$, and $V_v = V_t+\pi\cdot d_p^3\cdot L/(12\cdot P_p\cdot P_f)$. The authors found that the changes of the three variables (T_v, ρ_v, and V_v) are small during the waiting period. Therefore, their manipulations on T_v, ρ_v and V_v are valid. However, the tunnel heat transfer heat (dQ_{tun}/dt) should be time dependent because the meniscus radius is changing during the bubble cycle. Therefore, the authors proposed that equation (21) be replaced by equation (22).

$$\int_0^{\Delta t_w} \frac{\mathrm{d}Q_{\mathrm{tun}}/\mathrm{d}t}{\Delta T_{\mathrm{ws}}}\,\mathrm{d}t = V_{\mathrm{vm}} i_{\mathrm{fg}} \left[\frac{\rho_v (i_{\mathrm{fg}} - R_g T_{\mathrm{vo}})}{R_g T_{\mathrm{vo}}^2} \times \ln\left(\frac{T_w - T_{\mathrm{vo}}}{T_w - T_{\mathrm{vl}}}\right) + \frac{\rho_v}{\Delta T_{\mathrm{tl}}} \ln\left(\frac{V_{\mathrm{vl}}}{V_t}\right)\right]. \quad (22)$$

The right-hand side of equation (22) can be explicitly calculated for a given wall superheat ΔT_{ws}. As noted previously, the present model accounts for the temporal variation of $(\mathrm{d}Q_{\mathrm{tun}}/\mathrm{d}t)$, by formulating the liquid thickness at each time step [equation (9)]. In the present model, the left-hand side of equation (22) was calculated using equations (9)–(12) with small time step increments ($\mathrm{d}t$) from the beginning to the end of the waiting period (Δt_w), until it equals the right hand side of equation (22).

Bubble growth period. For a plain surface, the bubble growth rate is controlled by inertia force, and the bubble growth is linearly proportional to time ($R \sim t$) at the early stage. Then, the growth rate is dominated by evaporation at the interface, which causes vapor addition to the bubble, and the bubble growth is characterized by, $R \sim t^{1/2}$ (Miyatake *et al.* [15]). Mikic and Rohsenow [16] have developed an equation for calculating bubble growth rate on plain surfaces, in the inertia and heat transfer regimes for pure refrigerant, and was extended by Miyatake *et al.* [15] for prediction of binary mixture.

As discussed by Chien and Webb [4], the bubble growth mechanism on the structured surface is different from that on a plain surface. For a structured surface, the evaporation on the bubble interface is not important because the vapor is mainly supplied from the subsurface tunnel. Therefore, inertia controlled bubble growth dominates the entire bubble growth period. For inertia controlled growth, Mikic and Rohsenow [16] assumed the growth of the bubble is controlled by the increasing vapor pressure of the vapor inside the bubble, and balanced by the inertia resistance and the surface tension on the liquid–vapor interface. They showed that the bubble growth is given by

$$\left(\frac{\mathrm{d}R}{\mathrm{d}t}\right)^2 = \frac{b}{\rho_l}\left(P_v - P_s - \frac{2\sigma}{R}\right) \quad (23)$$

where $b = 2/3$ for a bubble growing in an infinite mass of liquid, or $b = \pi/7$ in equation (23) for a spherical bubble growing attached to a surface. The viscous force is neglected in the above equation. Using the Clausius–Clapeyron equation to relate the pressure difference $(P_v - P_s)$ to the corresponding temperature difference, and neglecting the pressure drop across the liquid–vapor interface $(2\sigma/R)$, Mikic and Rohsenow [16] changed equation (23) to

$$\left(\frac{\mathrm{d}R}{\mathrm{d}t}\right)^2 = \left(\frac{\pi}{7}\frac{i_{\mathrm{fg}}\rho_v \Delta T_{\mathrm{ws}}}{\rho_l T_s}\right)\left(\frac{T_v - T_s}{T_w - T_s}\right). \quad (24)$$

As indicated by Mikic and Rohsenow [16], T_v may be any value between T_s and T_w, depending on the conditions presented in the considered growth.

Nakayama *et al.* [6] modified equation (23) to calculate the bubble growth period for structured surfaces. They concluded that $(P_v - P_s)$ is negligible, based on the assumption $R \gg d_p/2$. However, the present authors find that the bubble growth period is four times greater than Nakayama's prediction. This is because bubble starts at $R = d_p/2$, as compared to the Nakayama *et al.* [6] assumption of $R \gg d_p/2$, which we feel is inappropriate. We also find that the bubble growth period increases as the wall superheat decreases. Therefore, the $(P_v - P_s)$, which depends on the wall super heat, is small but is not negligible.

For the structured surface, the pressure drop across liquid–vapor interface $(2\sigma/R)$ should not be neglected, and $(P_v - P_s)$ should be of the same order of the 'breakthrough pressure' $(4\sigma/d_p)$. It is also reasonable to assume that the $(P_v - P_s)$ increases as the wall superheat $(T_w - T_s)$ increases. Therefore, one gets

$$\frac{\mathrm{d}R}{\mathrm{d}t} = \left(\frac{\pi}{7}\frac{i_{\mathrm{fg}}\rho_v \Delta T_{\mathrm{ws}}}{\rho_l T_s}\right)^{1/2}\left(\frac{(T_v - T_s) - 2\sigma/(mR)}{T_w - T_s}\right)^{1/2} \quad (25)$$

where

$$T_v - T_s - 2\sigma/(mR) = \left(\frac{T_w - T_s}{T_w^* - T_s}\right)\left(\frac{4\sigma}{md_p} - \frac{2\sigma}{mR}\right)$$

where $m = \mathrm{d}P/\mathrm{d}T$ at T_s, and T_w^* is a reference wall temperature. At $T_w = T_w^*$, the vapor superheat $\Delta T_{vs} = 4\sigma/(\mathrm{m}d_p)$. The authors linearized R in the second term on the right side of equation (25) and get

$$\left(\frac{\mathrm{d}R}{\mathrm{d}t}\right) = \left(\frac{\pi i_{\mathrm{fg}}\rho_v \Delta T_{\mathrm{ws}}}{7\ \rho_l T_s}\right)^{1/2} C_{\mathrm{tg}}\left(\frac{d_b - d_p}{d_b + d_p}\right)^{1/2} \quad (26)$$

where

$$C_{\mathrm{tg}} = \left[\frac{4\sigma}{md_p(T_w^* - T_s)}\right]^{1/2}.$$

The C_{tg} is a dimensionless parameter, which represents the slope of vapor superheat vs. the reference wall superheat $(T_w^* - T_s)$. Since T_w^* is an unknown, the authors assume C_{tg} in equation (26) is an empirical constant, and find it by curve fitting from the bubble growth data [4]. The authors found that $C_{\mathrm{tg}} = 0.0296$ best fits the data. Setting the boundary conditions for equation (26): $R = d_p/2$, at the beginning, and $R = d_b/2$ at the end of the growth period, one gets

$$\Delta t_g = 0.0296\left[\frac{7}{\pi}\frac{\rho_l T_s}{i_{\mathrm{fg}}\rho_v \Delta T_{\mathrm{ws}}}\frac{(d_b + d_p)}{(d_b - d_p)}\right]^{1/2}\left(\frac{d_b - d_p}{2}\right). \quad (27)$$

Nucleation site density

The vapor generated in the tunnel is ejected through the surface pores. The bubble diameter and frequency are predicted as discussed above. From an energy balance, $q''_{tun} = i_{fg} \cdot V_v \cdot \rho_v$. From a mass balance, one can get the nucleation site density (n_s) by the following equation.

$$n_s = \frac{q''_{tun}}{\rho_v i_{fg} f(\pi d_b^3)/6}. \qquad (28)$$

External heat flux

The Haider and Webb [11] model is used for the prediction of the external heat flux. They assume the heat transfer outside the tunnel is controlled by two asymptotes. The first asymptote is the heat transfer due to transient conduction ($q''_{ex,MR}$), which was solved (Mikic and Rohsenow [17]) as given by equation (29).

$$q''_{ex,MR} = n_s Q_{bub} = f\int_0^{1/f}\left(-k_l \pi d_b^2 \frac{\partial T}{\partial y}\right)_{y=0} dt$$
$$= 2\sqrt{\pi}\sqrt{k_l \rho_l c_p}\sqrt{f} d_b^2 n_s (T_w - T_s). \qquad (29)$$

The second asymptote is due to steady state convection due to agitation of the departing bubble. Haider and Webb [11] show that the external heat flux is given by

$$q''_{ex} = q''_{ex,MR}\left[1+\left(\frac{0.66\pi c}{Pr^{1/6}}\right)^2\right]^{1/2} \qquad (30)$$

where the empirical constant of $c = 6.42$, was curve fitted from the Chien and Webb [4] and Nakayama *et al.* [8] bubble formation data. The prediction is within ±25%. As suggested by Haider and Webb [11], this constant is universal, and can be used for different fluids and geometric dimensions.

For prediction of external heat flux on structured surfaces, the bubble dynamic factors (d_b, f, n_s) needed in the Haider and Webb [11] model are given by equations (19), (22), (27), (28).

Prediction procedure

The present model predicts the total heat flux (q'') for given wall superheat (ΔT_{ws}) and dimensions (d_b, P_p, P_f, H_t), by the following procedure.

(1) Calculate the departure diameter (d_b) for given d_p and fluid properties by equation (19).
(2) Calculate the bubble growth period (Δt_g) by equation (27) for given ΔT_{ws} and fluid properties, using d_b obtained in step 1.
(3) Calculate the initial liquid meniscus radius, $R_{m,i}$ by equation (13), using a correlation [see equation (31)] for prediction of $\Delta A_{l,cyc}$.
(4) Calculate the latent heat transferred in the tunnels during the bubble cycle by integrating equations (9) and (10) with stepwise decreasing R_m from $R_{m,i}$ to $R_{m,e}$. The Δt during one increment of r_m is found by equations (11) and (12).
(5) Calculate the waiting period (Δt_w) by equations (9)–(12) and (22), and find the meniscus radius ($R_{m,g}$) at the beginning of the bubble growth period.
(6) Continue the calculation of the tunnel heat flux as for the bubble growth period, and calculate by decreasing R_m for $\Delta t_w < t < \Delta t_w + \Delta t_g$.
(7) Sum the tunnel heat flux (q''_{tun}) during the waiting period (Δt_w) and bubble growth period (Δt_g) for given d_p, P_p, P_f, H_t, ΔT_{ws} and fluid properties, and get the bubble frequency, $f = 1/(\Delta t_w + \Delta t_g)$.
(8) Use equation (28) to calculate the nucleation site density (n_s) from q''_{tun} and d_b obtained in step 1 and 2, and f obtained in step 7.
(9) Calculate the external heat flux (q''_{ex}) by equation (30) for a given ΔT_{ws} and d_b, f, n_s, obtained in step 2, 7 and 8.
(10) Calculate total heat flux $q'' = q''_{ex} + q''_{tun}$.

Correlation of $\Delta A_{l,cyc}$

The above prediction procedure requires the initial meniscus radius, $R_{m,i}$. As given by equation (13), the $R_{m,i}$ is analytically related to $R_{m,e}$ and $\Delta A_{l,cyc}$. The $R_{m,e}$ is given by equations (9)–(12) and (22). The $\Delta A_{l,cyc}$ is predicted by a correlation. This correlation is obtained by curve fitting the R-11, R-123, R-134a, and R-22 experimental data given in Chien *et al.* [1–3, 13] to obtain experimental $R_{m,i}$ and $\Delta A_{l,cyc}$ data. The ranges of parameters in the data base are listed in Table 1.

The model assumes the menisci occupy the entire tunnel length. When only part of the tunnel is flooded (at low heat fluxes), or the meniscus vanishes ($q'' > q''_{DHF}$), the model will result in over prediction. Hence, the data for $q'' < 0.2 \cdot q''_{DHF}$ or $q'' > q''_{DHF}$ were excluded from the correlation for $R_{m,i}$. As discussed by Chien and Webb [1, 2] the dry out heat flux, q''_{DHF}, is defined as the heat flux where the heat transfer coefficient approaches maximum value. Different from CHF (critical heat flux), which defines the condition for the dry out of a plain boiling surface, the q''_{DHF} defines the dry out condition inside the tunnels of structures surfaces. When $q'' > q''_{DHF}$, liquid is depleted in the tunnel, and the heat transfer coefficient drastically decreases.

The experimental $R_{m,i}$ data base is obtained by guessing $R_{m,i}$ in step 2 of the aforementioned pre-

Table 1. Range of parameters in the data base

Reference	Fluids	d_p (mm)	P_p (mm)	fins m	W_t (mm)	H_t (mm)
[1, 2]	R11, R123	0.12–0.28	0.75–1.5	1378, 1575, 1968	0.25–0.4	0.5–1.5
[3, 14]	R134a, R22	0.18–0.28	0.75–1.5	1575, 1968	0.25–0.33	0.6–1.5

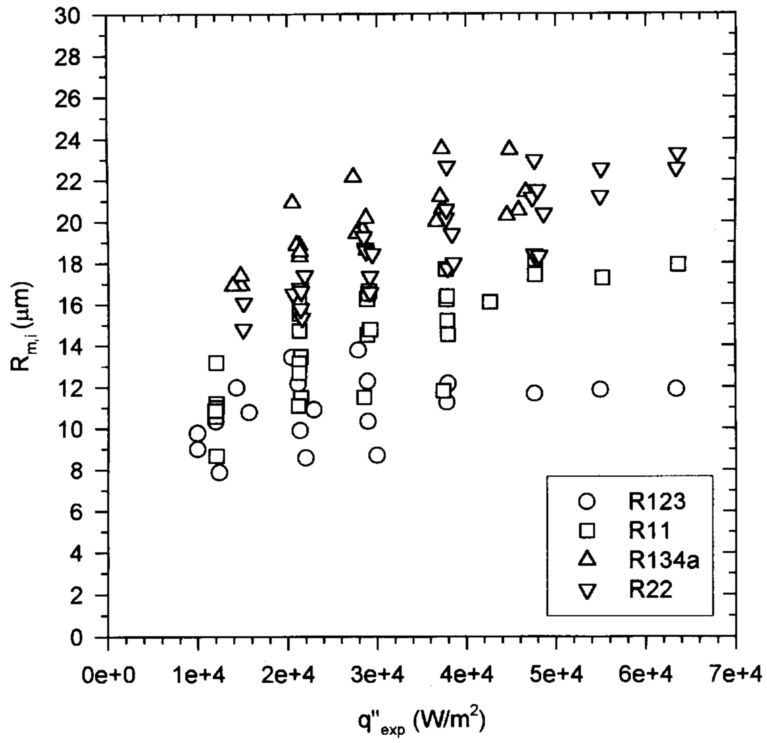

Fig. 4. Initial meniscus radius ($R_{m,i}$) evaluated from experimental data.

diction procedure. Each $R_{m,i}$ corresponds to a q''_{pred}. Change $R_{m,i}$ and repeat step 1–11 until the prediction for q'' at a given ΔT_{ws} agrees with experimental data ($q''_{pred} = q''_{exp}$). The resulting calculated $R_{m,i}$ data are shown in Fig. 4. Then, the experimental $\Delta A_{l,cyc}$ data are calculated by equation (13). The next step involved developing a correlation for $\Delta A_{l,cyc}$ as a function of the geometry, and fluid dependent parameters.

The $\Delta A_{l,cyc}$ represents the amount of liquid that flows into the tunnel during one bubble cycle. The understanding of the boiling mechanism from the parametric experiments (Chien *et al.* [1–3, 13]) provide the following information to define the dependent parameters in the correlation of $\Delta A_{l,cyc}$.

(1) Geometric parameters: pore diameter (d_p), pore pitch (P_p), tunnel height (H_t), tunnel width (W_t), and tunnel pitch (P_t) are important parameters. The present model included these parameters in the calculation of tunnel heat transfer and waiting period. The dependencies of pore diameter, tunnel width and tunnel height are also found in the $R_{m,i}$ correlations.

(2) Wall superheat (ΔT_{ws}): more liquid is evaporated and generate more bubbles at greater wall superheat ΔT_{ws}. Therefore, the liquid intake activity and the $\Delta A_{l,cyc}$ is dependent on ΔT_{ws}.

(3) Fluid properties: because the liquid flows into the tunnel through the small surface pores, one would expect the liquid flow rate to depend on liquid viscosity (μ_l). The liquid is pulled into the corners by surface tension force. Hence, $\Delta A_{l,cyc}$ is also dependent on surface tension, σ.

Based on the above thoughts, the following correlation for $\Delta A_{l,cyc}$ was found to predict within 19% MSD using the $R_{m,i}$ data shown in Fig. 4.

$$\Delta A_{l,cyc} = \frac{4-\pi}{2} C_{Rm} \Delta T_{ws}^{n1} d_p^{n2} (H_t + W_t)^{n3} \left(\frac{\sigma^{n5}}{\mu_l^{n4}}\right). \tag{31}$$

A number of possible correlations are evaluated before the best correlation was chosen. The empirical constants used in equations (31) are given in Table 2, and the units of variables are given in the nomenclature list. Table 2 is applicable to all fluids and for arbitrary geometric dimensions within the range of the present experiments, except the 1575–0.6r tube, which has a rectangular fin base. The available data are not sufficient to obtain the correlation of $R_{m,i}$ for the rectangular fin base tubes.

Table 2. Values of the empirical constants using data at ($0.2 \cdot q''_{DHF}) < q'' < q''_{DHF}$

C_{Rm}	$n1$	$n2$	$n3$	$n4$	$n5$
4.71E-9	0.1882	0.609	1.49	1.7712	0.512

VERIFICATIONS OF ASSUMPTIONS

The aforementioned database for $R_{m,i}$, calculated from experimental data, provides important information to evaluation of the major assumptions in our model.

Thin liquid film on the tunnel walls

The present model assumes that the evaporation occurs only on the liquid menisci in the corners. However, one may speculate that thin liquid films also exist on the tunnel side walls, and affect the tunnel evaporation rate. The evaporation rate is proportional to k_l/δ. A thin film on the side walls will evaporate more quickly than the thicker liquid menisci. Assuming a uniform liquid film thickness on the side wall, Chien [3] found that this film would evaporate in approximately 10^{-5} s, which is less than 5% of the typical waiting period. The predicted waiting period agrees with the Chien and Webb [4] data only if the amount of liquid evaporated in thin films on the side walls is less than 3% of that in the menisci. Hence, the authors concluded that any evaporation that occurs in thin films on the side walls is negligible compared to that evaporated in the menisci. The model includes only evaporation of the liquid menisci.

Liquid spreading inside the tunnel

The present model assumes that the entering liquid is retained in the corners at the fin tips. This assumption is verified by envisioning the liquid spreading process during the liquid intake period as illustrated in Fig. 5.

At the end of a bubble cycle, liquid is drawn into the tunnel by inertia force. Then, liquid moves into the corners and spreads along the tunnel length by surface tension force. Liquid is pulled from point A to point B by surface tension force due to the meniscus radius variation along the tunnel length (the x-direction on Fig. 5). As shown in Fig. 5, the liquid meniscus radius at point A ($R_{m,A}$) is greater than at point B ($R_{m,B}$). Using the analysis of Adamek and Webb [18] for the liquid–vapor interface surface tension effect, Chien [3] showed that the average liquid flow velocity along the tunnel length (x-direction in Fig. 5) is given by

$$u_{x,\mathrm{ave}} = \frac{1}{\mu_l}\frac{\mathrm{d}p}{\mathrm{d}x}\frac{\delta^2}{3} \tag{32}$$

where

$$\frac{\mathrm{d}p}{\mathrm{d}x} = -\sigma\frac{\mathrm{d}(1/r)}{\mathrm{d}x}$$

where $1/r$ is the curvature of the liquid vapor interface, and x is the coordinate along the tunnel length. He assumed a linear variation of meniscus curvature from point A (where the curvature radius, $R_{m,A} = R_{m,i}$) to point B (where $R_{m,B} = R_{ne}$) as shown in Fig. 5. Applying typical values of $R_{m,i}$ and R_{ne} from the experimental data, he used equation (32) to find $u_{x,\mathrm{ave}} = 800$ mm s^{-1}. Therefore, the liquid can move quickly in the x-direction. From a similar analysis, Chien [3] found the surface tension induced velocity in the s-direction (toward the fin tip) is about 30 mm s^{-1}. Therefore, the liquid velocity in the s-direction (toward the fin base) is less than the x-direction. This is supportive of the assumption of uniform liquid thickness along the tunnel length.

An important consideration in the model is the possibility that liquid menisci may also exist at the fin base. Liquid entering at the surface pore will be acted on by surface tension force, which will tend to retain liquid in the small menisci at the fin tip. However, liquid inertia will also try to spread the liquid along the fin side walls. Once the liquid is on the side wall, surface tension force will pull liquid into the corners at the fin base. For a rectangular fin base, we believe that more liquid will be retained at the fin tip than at the fin base. For a circular fin base, the meniscus radius is much larger than that at the fin tips, as shown in Figs 1 and 6. The fin base radius (R_b) for circular fin base tubes is 0.14–0.19 mm as shown in Table 3. Hence, the amount of liquid pulled to the fin base will be substantially less for a circular fin base than for a rectangular fin base. Based on the previous considerations, the present model assumes that only two

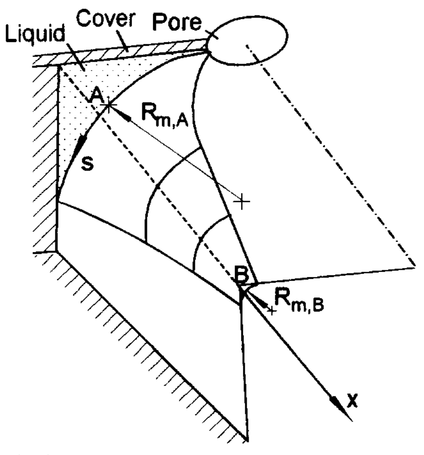

Fig. 5. Liquid motion in the corners along the tunnel length.

(a) Circular fin base **(b) Rectangular fin base**

Fig. 6. Fin base shapes. (a) Circular fin base (1575–0.6 tube); (b) Rectangular fin base (1575–0.6r tube).

Table 3. Fin base radius

Tube (fins m-H_t)	1575–0.6r	1575–0.6	1575–0.8	1575–1.5	1968–0.7	1968–0.9
R_b (mm)	0.01	0.19	0.17	0.16	0.15	0.14

liquid menisci exist for the circular fin base tunnel ($N_m = 2$), and that they are at the fin tip.

For the case of the tunnel having rectangular fin base, the fin base radius (R_b) for the 1575–0.6r tube is 0.01 mm, which is smaller than the typical meniscus radius. Therefore, two more liquid menisci may exist in the corners at the base of the fins. Chien and Webb [1] show that a surface having a rectangular fin base has higher performance than an identical surface having a circular fin base. We believe that this is because of the liquid menisci that exist at the fin base. This geometry configuration is not addressed in the present model.

PREDICTIVE ABILITY OF THE PRESENT MODEL

The present model was used to predict the Chien *et al.* [1–3, 13] data for $q'' = 20$–100% of the q''_{DHF}. These data include R-11, R-123, R-134a and R-22 pool boiling data on tubular surfaces having a circular fin base for heat fluxes between 10–65 kW m^{-2}. The range of geometric parameters are shown in Table 1. The results are shown in Fig. 7. Figure 7 shows that the heat flux is predicted within $\pm 33\%$ absolute error (MSD = 0.20), except for the dark symbols, at quite low heat fluxes. The model over predicted these dark points, because some tunnels become partially liquid filled and do not generate bubbles at low heat flux. These liquid filled tunnels should be considered 'non-active'. The effective tunnel inside surface area decreases when tunnels are partially flooded. It is possible that one may predict the length of the liquid filled region as a function of heat flux. However, this was not attempted in the present work.

The present model predicts bubble frequency and departure diameter quite well, as shown by Figs. 8 and 9. As shown in Fig. 8, the model predicts the bubble frequencies of Chien and Webb [4] experimental data for R-123 on four surfaces within $\pm 30\%$ absolute error (MSD = 15%). Figure 9 shows the error in predicted bubble departure diameter $(d_{b,\mathrm{pred}} - d_{b,\mathrm{exp}})/d_{b,\mathrm{exp}}$. The Chien and Webb [4] data for R-123 is predicted within $\pm 12\%$ (MSD = 7%). Recall that the effect of the heat flux on bubble departure diameter is not considered in the model. Figure 9 shows a quite small effect of heat flux on bubble departure diameter. Table 4 compares the experimental data from Nakayama *et al.* [8] and the Chien [3] data on water, methanol, R-11, and R-123. The present model was able to predict d_b for all the fluids within $\pm 20\%$.

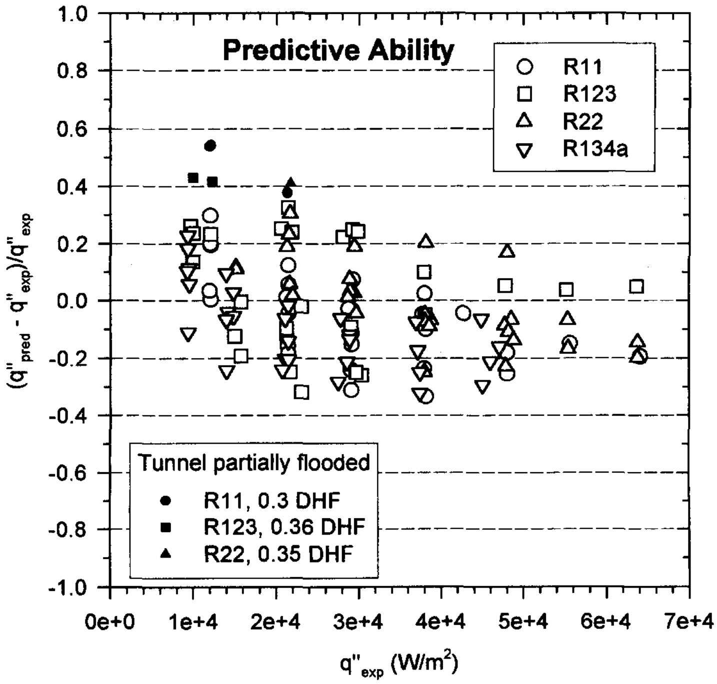

Fig. 7. Predictive error on total heat flux.

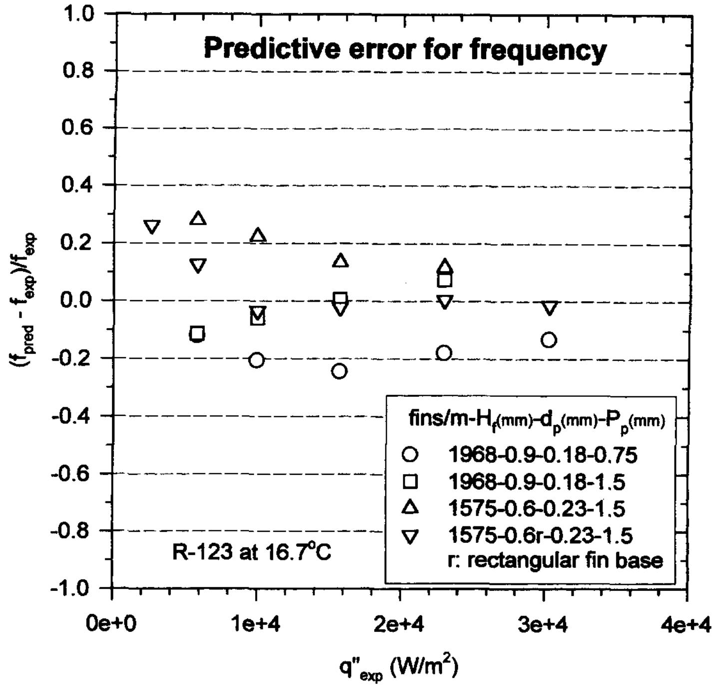

Fig. 8. Predictive error on bubble frequency.

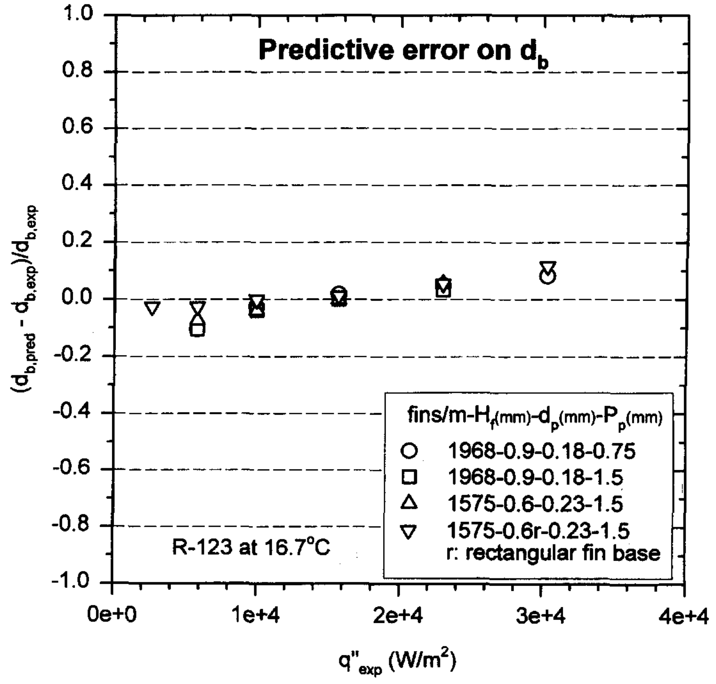

Fig. 9. Predictive error on bubble departure diameter.

CONCLUSIONS

(1) A semi-analytical model is proposed for pool boiling on structured surfaces having a circular fin base. The model assumes evaporation from liquid menisci at the top of the fins and is applicable to surfaces having a circular fin base and an arbitrary combination of d_p, P_p, P_f, H_t. It can predict most boiling heat transfer data for four refrigerants (R-11, R-123, R-134a, and R-22) within ±33% (0.20 MSD).

(2) Bubble departure diameter and bubble frequency

Table 4. Comparisons of predictions and data for bubble departure diameter

Reference	Fluid	d_p (mm)	$d_{b,exp}$ (mm)	$d_{b,pred}$ (mm)
[6]	Water at 1 atm	0.1	0.78 ± 0.1	0.78
[6]	R11 at 1 atm	0.1	0.7 ± 0.1	0.53
[3]	R11 at 26.7°C	0.23	0.8 ± 0.1	0.80
[3]	Methanol, 1 atm	0.23	1.1 ± 0.1	0.96
[3]	R123 at 26.7°C	0.23	0.77 ± 0.1	0.76
[3]	R123 at 26.7°C	0.18	0.72 ± 0.1	0.67

are included in the present model. The predictions are within $\pm 20\%$ absolute error (MSD = 0.07) for the bubble departure diameter, and within ± 30 absolute error (MSD = 0.15) for the bubble frequency.

(3) The present model is the first one that includes temporal variation of evaporation rate inside the tunnel.

(4) The initial meniscus radius ($R_{m,i}$) was calculated using heat transfer data based on the present model. By comparing the meniscus radius and fin base radius, we concluded that a rectangular fin base shape will likely yield greater boiling performance because of contributions from meniscus evaporation at the fin base.

(5) The modeling on d_b, f, n_s allowed use of the Haider and Webb [11] model for the q''_{ex} term in equation (1).

Acknowledgements—We are thankful to Carrier Corp., Olin Brass Corp., Showa Aluminum Co., The Trane Co., UOP Corp., York International, Wieland-Werke AG, and Wolverine Tube, for supporting this work.

REFERENCES

1. Chien, L.-H. and Webb, R. L., Parametric studies of nucleate pool boiling on structured surfaces, Part I: effect of tunnel dimensions, HTD-Vol. 326. *National Heat Transfer Conference*, 1996, **4**, 129–136.
2. Chien, L.-H. and Webb, R. L., Parametric studies of nucleate pool boiling on structured surfaces, Part II: effect of pore diameter and pore pitch, HTD-Vol. 326. *National Heat Transfer Conference*, 1996, **4**, 137–143.
3. Chien, L.-H., Mechanism and analysis of nucleate boiling on structured surfaces. Ph.D. thesis, Department of Mechanical Engineering, Penn State University, University Park, PA, 1996.
4. Chien, L.-H. and Webb, R. L., Measurement of bubble dynamics on an enhanced boiling surface. Accepted for publication in *Experimental Thermal and Fluid Science*, 1998.
5. Chien, L.-H. and Webb, R. L., Visualization experiments of pool boiling on enhanced surfaces. Accepted for publication in *Experimental Thermal and Fluid Science*, 1998.
6. Nakayama, W., Daikoku, T., Kuwahara, H. and Nakajima, T., Dynamic model of enhanced boiling heat transfer on porous surfaces Part II: analytical modeling. *Journal of Heat Transfer*, 1980, **102**, 451–456.
7. Haider, I., A theoretical and experimental study of nucleate pool boiling enhancement of structured surfaces. Ph.D. thesis, Department of Mechanical Engineering, Penn State University, University Park, PA, 1994.
8. Nakayama, W., Daikoku, T., Kuwahara, H. and Nakajima, T., Dynamic model of enhanced boiling heat transfer on porous surfaces Part I: experiment investigation. *Journal of Heat Transfer*, 1980, **102**, 445–450.
9. Arshad, J. and Thome, J. R., Enhanced boiling surfaces: heat transfer mechanism mixture boiling. *Proc. ASME–JSME Therm. Eng. Joint Conf.*, 1983, **1**, 191–197.
10. Ayub, Z. H. and Bergles, A. E., Pool boiling from GEWA surfaces in water and R-113. *Wärme- und Stoffübertragung*, 1987, **21**, 209–219.
11. Haider, I. and Webb, R. L., A transient micro-convection model of nucleate pool boiling on plain surfaces. To be published in *International Journal of Heat and Mass Transfer*, 1997, **40**, 3675–3688.
12. DasGupta, S., Schonberg, J. A., Kim, Y. and Wayner, P. C., Use of the augmented Young–Laplace equation to model equilibrium and evaporating extended menisci. *Journal of Colloid and Interface Science*, 1993, **157**, 332–342.
13. Chien, L.-H., Zharnescu, V. and Webb, R. L., Effect of pore diameter and pore pitch for pool boiling on structured surfaces using R-134a and R-22. *Journal of Enhanced Heat Transfer*, submitted.
14. Kolev, N. I., The influence of mutual bubble interaction on the bubble departure diameter. *Experimental Thermal and Fluid Science*, 1994, **8**, 167–174.
15. Miyatake, O., Tanaka, I. and Lior, N., A simple universal equation for bubble growth in pure liquids and binary solutions with a non-volatile solute. *International Journal of Heat and Mass Transfer*, 1997, **40**(7), 1577–1584.
16. Mikic, B. B. and Rohsenow, W. M., Bubble growth rates in non-uniform temperature field. *Prog. in Heat and Mass Transfer*, 1969, **2**, 283–292.
17. Mikic, B. B. and Rohsenow, W. M., A new correlation of pool-boiling data including the effect of heating surface characteristics. *Journal of Heat Transfer*, 1969, **91**, 245–250.
18. Adamek, T. A. and Webb, R. L., Prediction of film condensation on horizontal integral-fin tubes. *International Journal of Heat and Mass Transfer*, 1990, **33**(8), 1721–1735.